A Dynamic Study of the Single Active Bridge Converter

Alberto Rodríguez, *Member, IEEE*, Alexis A. Gómez, *Student Member, IEEE*,
Marta M. Hernando, *Senior Member, IEEE*, Diego G. Lamar, *Senior Member, IEEE*,
and Javier Sebastián, *Life Senior Member, IEEE*

***Abstract*—In this article, a thorough study of the dynamic behavior of the single active bridge (SAB) converter is presented. The SAB converter can be considered a unidirectional version of the dual active bridge (DAB) converter, which has been extensively analyzed in recent years. However, the dynamics of the SAB converter differs from the one corresponding to the DAB converter and has not been addressed so far. The SAB converter can operate in two different conduction modes, namely discontinuous conduction mode (DCM) and continuous conduction mode (CCM). The SAB operating in DCM presents the same static and dynamic behavior as the phase-shifted controlled full bridge (PSFB) converter if the value of the inductor of the SAB is the same as the value of the output inductor of the PSFB referred to the transformer primary side. However, the dynamic behavior of the SAB converter in CCM is different and must be analyzed in detail. As a result of the analysis carried out, average small-signal linear models have been obtained for both conduction modes. These models are compared with the ones obtained for other similar converters and they have been validated with simulation and experimental results.**

***Index Terms*—Dual active bridge converter, isolated dc–dc converters, single active bridge converter, small-signal linear model.**

I. INTRODUCTION

DUAL active bridge (DAB) converter is one of the most attractive bidirectional dc–dc converters [1], [2], [3], [4]. It has been widely proposed for applications with bidirectional power flow. However, the secondary active bridge can be replaced with a diode-based bridge in the case of unidirectional power flow applications, thus simplifying the overall converter. The converter, thus, obtained is referred as the single active bridge (SAB) converter and exhibits higher power density, reliability, and lower cost, at expense of losing the bidirectional power flow capability. Additionally, the SAB shows remarkable resemblance to the phase-shifted full bridge (PSFB), the only difference being that an inductor is placed at the output in the case of the PSFB. As the SAB converter does not have the mentioned inductor, there is one less magnetic element, and the remainder magnetic elements can be integrated into one. This results in higher power density. Moreover, the voltage withstood by the output diodes is clamped to that of the output voltage. Potential applications of the SAB converter are those that require galvanic isolation and unidirectional power flow capabilities, especially those with a high output voltage such as renewable energies and fast charging of electric vehicles [5], [6]. Another alternative converter for similar applications can be the full-bridge *LLC* converter. However this converter is regulated by varying the switching frequency, which is considered a disadvantage in some cases.

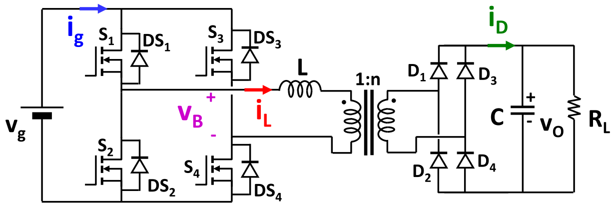

Fig. 1. Single active bridge converter.

The general scheme of the SAB converter is shown in Fig. 1. Its static analysis has been carried out in [7], [8], [9], and [10]. The SAB converter can operate in two conduction modes according to the inductor current (i_L) waveform, as shown in Fig. 2 and [7]. If current i_L crosses zero and does not remain at this value, the converter operates in the continuous conduction mode (CCM). On the contrary, if current i_L remains at zero during a part of the switching period, the converter operates in the discontinuous conduction mode (DCM).

In the case of the DAB converter, small-signal average linear models can be found in several publications (i.e., [4] and [10]). Additionally, large and small-signal models for the single active half-bridge (SAHB) converter are developed in [10]. This converter, however, can only operate in the DCM or in the border between this mode and CCM, due to the half-bridge structure in the converter primary side, instead of the classical full-bridge one. A more detailed analysis of the differences between the dynamic models proposed in this article for the SAB converter

---

Received 16 February 2024; revised 14 May 2024; accepted 6 July 2024. Date of publication 11 July 2024; date of current version 28 January 2025. This work was supported in part by the European Union under Grant UE-23-POWERIZED-101096387, in part by the Spanish Government under Grant MCINN-22-TED2021-130939B, and in part by the Principality of Asturias grant "Severo Ochoa" under Grant BP21-114. Recommended for publication by Associate Editor D. Costinett. *(Corresponding author: Alexis A. Gómez.)*

The authors are with the Power Supply Systems Group, University of Oviedo, 33003 Oviedo, Spain (e-mail: rodriguezalberto@uniovi.es; gomezalexis@uniovi.es; mmhernando@uniovi.es; gonzalezdiego@uniovi.es; sebas@uniovi.es).

Color versions of one or more figures in this article are available at https://doi.org/10.1109/TPEL.2024.3426590.

Digital Object Identifier 10.1109/TPEL.2024.3426590

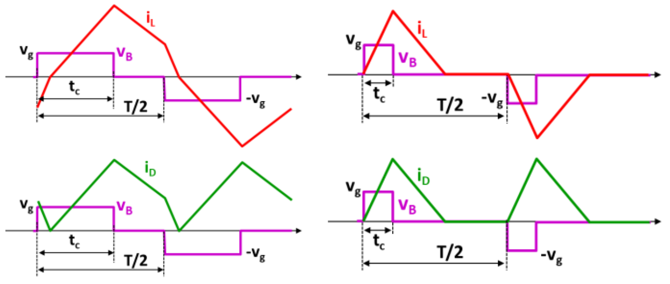

(a) (b)

Fig. 2. Current through the inductor (i_L), current injected into the R_LC network (i_D), and voltage generated by the active bridge (v_B). (a) In the CCM. (b) In the DCM.

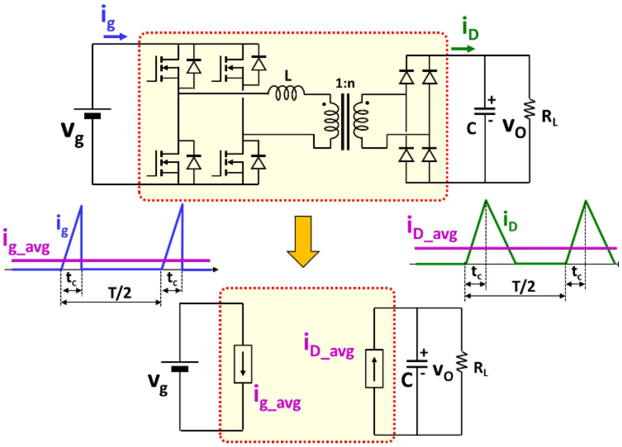

Fig. 3. CIECA method applied to the SAB converter.

and those proposed in previous papers for similar converters (such as SAHB and DAB) is provided in Section V.

In this article, small-signal linear models for the different conduction modes of the SAB converter have been obtained and validated using simulation and experimental results. Special attention has been paid to analyze whether the value of the average current injected into the output R_LC network is updated each switching half-period, which is of primary concern to obtain a simple small-signal linear model. As will be explained, the situation is clearly different in the case of operation in the CCM in comparison with the case of operation in the DCM. To address this issue, special attention must be paid to the current and voltage waveforms shown in Fig. 2. Current i_D is the current injected into the R_LC network and corresponds to a rectified and scaled version of i_L. It should be noted that this waveform differs from the current injected into the R_LC network in the case of the DAB converter. As shown in Fig. 2, i_L is zero at the beginning of the switching half-period when the converter operates in DCM. However, the value of i_L at the beginning of the switching half-period is not zero when the converter operates in the CCM. Consequently, the electric charge transferred to R_LC in DCM is independent of the previous switching half-period. This implies a cycle-by-cycle update of the transferred power that finally leads to a first order dynamic model. This is the same situation as the one corresponding to other similar converters, such as the PSFB or the Buck converter operating in the very well-known classical DCM. In the latter case, the update process takes place each switching period.

On the other hand, the value of i_L at the beginning of one switching half-period depends on its value at the end of the previous one if the SAB converter is operating in the CCM, as Fig. 2(a) shows. Consequently, a higher order dynamic model could be expected, and a deeper analysis must be carried out to obtain the dynamic behavior of the SAB converter in the CCM.

II. AVERAGE MODEL OF THE SAB CONVERTER

The SAB converter shown in Fig. 1 can be divided into three parts: 1) the input voltage source, 2) the set of switches and magnetic elements, and 3) the R_LC output network. Various methods can be used to derive the large and small signal models such as the generalized average modeling [11] or discrete time modeling [12]. However, because its simplicity, the method used to obtain the small-signal linear average models of this converter is the well-known current injected equivalent circuit approach (CIECA), explained in [13] and [14]. The basic idea of CIECA, represented in Fig. 3, is to replace the converter with a two-port device made up of two nonlinear current sources. These current sources must behave in the same way as the average converter currents that they replace. Thus, the value of the input current source coincides with the average input current, i_{g_avg}, whereas the value of the output current source coincides with the average current injected into the R_LC network by the secondary diode bridge, and it is called i_{D_avg}. It should be noted that the obtained model exhibits the sampling delay characteristic of the averaging process. This delay will only be noticeable when trying to visualize variations close to the switching frequency of the converter and, therefore, this effect will be neglected for the model, as in most of the other average models [13], [14], [15]. Neglecting this delay is not a problem when using this model to tune linear control loops, as the crossover frequencies of those loops are orders of magnitude below the switching frequency.

A. Average Model in the DCM

Considering the waveform of i_D shown in Fig. 2(b) and the steady-state modeling presented in [7], we can easily obtain

$$i_{D\_avg} = \frac{v_g}{LTv_o}\left[v_g - \frac{v_o}{n}\right] t_c^2 \tag{1}$$

where T is the switching period, L is the inductor value, n is the transformer turns ratio, v_g is the input voltage, v_o is the output voltage, and t_c corresponds to the simultaneous conduction interval of either S_1 and S_4 or S_2 and S_3.

By considering the power balance in a switching period, we obtain

$$i_{g\_avg} = \frac{v_o}{v_g} i_{D\_avg} = \frac{1}{LT}\left[v_g - \frac{v_o}{n}\right] t_c^2. \tag{2}$$

Equations (1) and (2) can be rewritten as a function of the converter duty cycle ($d = \frac{t_c}{T}$), as follows:

$$i_{D\_avg} = \frac{Tv_g}{Lv_o}\left[v_g - \frac{v_o}{n}\right]d^2 \tag{3}$$

$$i_{g\_avg} = \frac{T}{L}\left[v_g - \frac{v_o}{n}\right]d^2. \tag{4}$$

It should be noted that these equations are valid not only in steady state, but also in transient response, because the energy stored in the inductor is zero both at the beginning and at the end of a switching half-period. In other words, there is an update of the value of these current sources each switching half-period. In fact, the vicinity of the switching frequency represents the limit of validity for this model.

Moreover, equations (3) and (4) show that the value of these current sources involves multiplications and divisions of variables such as d, v_g and v_o, which implies a nonlinear model. Therefore, classical transfer functions cannot directly be obtained from these equations and a linearization of the current sources around an operating point is needed. However, the linearization makes the new model only valid for small-signal analysis.

B. Average Model in the CCM

According to [7] and the waveforms given in Fig. 2(a), and following the same procedure as the one followed for the DCM, we can easily obtain the values of i_{D_avg} and i_{g_avg} for the CCM:

$$i_{D\_avg} = \frac{T}{2Ln}\left[v_g d - v_g d^2 - \frac{v_o^2}{4n^2 v_g}\right] \tag{5}$$

$$i_{g\_avg} = \frac{T}{2Ln}\left[v_o d - v_o d^2 - \frac{v_o^3}{4n^2 v_g^2}\right]. \tag{6}$$

It should be emphasized that, strictly speaking, these equations are only valid in steady state. This is due to the fact that these equations do not reflect any delays between a change in d and the resulting change in i_{D_avg} and in i_{g_avg}. According to these equations, the value of the current sources should be updated instantaneously when a change in d takes place, but this is not true. For example, the value of i_{D_avg} is obtained by averaging i_D, whose initial value depends on the previous switching half-period. Therefore, an update of i_{D_avg} each switching half-period is not possible. Consequently, the average model given for (5) and (6) is not valid for transient response, at least strictly speaking. Fortunately, in normal operating conditions, the value of these current sources will be updated in a few switching periods, as will be explained later. Thus, these equations can be used in transient events with minimal error. Therefore, this model will be extremely useful to obtain the small-signal average linear model in a similar way to the case of the operation in the DCM. For this purpose, a linearization of the current sources around the operating point must be carried out, also as in the case of DCM operation.

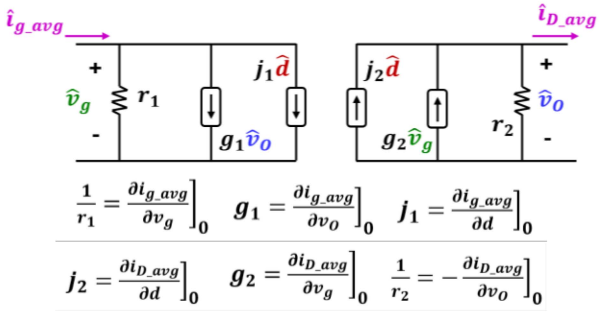

Fig. 4. Canonical small-signal linear circuit.

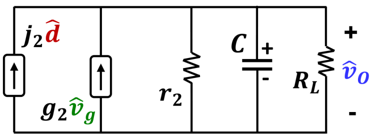

Fig. 5. Circuit used to calculate transfer functions.

III. SMALL-SIGNAL AVERAGE LINEAR MODEL OF THE SAB CONVERTER

The linearization process transforms the two-port device given in the yellow box of Fig. 3 into the one shown in Fig. 4, where the variables in capital letters correspond to the operating point, whereas the ones with a circumflex accent (hat) correspond to the small-signal perturbations.

A. Small-Signal Average Linear Model in the DCM

When operating in the DCM, the expressions of the parameters that define the current sources and the resistors given in Fig. 4 can be easily obtained by linearizing (3) and (4). The values thus obtained are shown in Table I, left-side column.

After connecting the $R_L C$ network at the output of the canonical circuit of Fig. 4, the circuit shown in Fig. 5 is obtained. Using this circuit, control to output voltage (G_{od}) and audio-susceptibility (G_{og}) transfer functions can be easily obtained

$$G_{od} = \left.\frac{\hat{v}_O}{\hat{d}}\right]_{\hat{v}_g=0} = \frac{j_2 R_{eq}}{1 + R_{eq}Cs} \tag{7}$$

$$G_{og} = \left.\frac{\hat{v}_O}{\hat{v}_g}\right]_{\hat{d}=0} = \frac{g_2 R_{eq}}{1 + R_{eq}Cs} \tag{8}$$

where

$$R_{eq} = \frac{R_L r_2}{R_L + r_2}. \tag{9}$$

From the values of j_2, g_2, and r_2 given in Table I for the DCM, (7) and (8) become

$$G_{od\ \mathrm{DCM}} = \left.\frac{\hat{v}_O}{\hat{d}}\right]_{\hat{v}_g=0} = \frac{\frac{2TV_g D V_o R_L}{R_L T D^2 V_g^2 + L V_o^2}\left(V_g - \frac{V_o}{n}\right)}{1 + \frac{L V_o^2 R_L}{R_L T D^2 V_g^2 + L V_o^2} Cs} \tag{10}$$

TABLE I
PARAMETERS OF THE CANONICAL CIRCUIT IN BOTH CONDUCTION MODES AND IN THE BOUNDARY BETWEEN THEM

	DCM	**Boundary in the DCM (N=2D)**	**Boundary in the CCM (N=2D)**	**CCM**
$\boldsymbol{j_1}$	$\frac{2TD}{L}\left[V_G-\frac{V_O}{n}\right]$	$\frac{TV_O}{nL}[1-N]$	$\frac{TV_O}{2nL}[1-N]$	$\frac{TV_O}{2Ln}[1-2D]$
$\boldsymbol{g_1}$	$-\frac{TD^2}{nL}$	$-\frac{TN^2}{4nL}$	$\frac{TN}{4nL}(1-2N)$	$\frac{T}{2nL}\left[D(1-D)-\frac{3}{4n^2}\left(\frac{V_O}{V_g}\right)^2\right]$
$\boldsymbol{\frac{1}{r_1}}$	$\frac{TD^2}{L}$	$\frac{TN^2}{4L}$	$\frac{TN^3}{4L}$	$\frac{T}{4n^3L}\left(\frac{V_O}{V_g}\right)^3$
$\boldsymbol{j_2}$	$\frac{2TV_gD}{LV_O}\left[V_G-\frac{V_O}{n}\right]$	$\frac{TV_O}{n^2NL}(1-N)$	$\frac{TV_O}{2n^2NL}(1-N)$	$\frac{TV_g}{2nL}[1-2D]$
$\boldsymbol{g_2}$	$\frac{TD^2}{L}\left[\frac{2V_G}{V_O}-\frac{1}{n}\right]$	$\frac{TN}{4nL}(2-N)$	$\frac{TN}{4nL}$	$\frac{T}{2nL}\left[D(1-D)+\frac{1}{4n^2}\left(\frac{V_O}{V_g}\right)^2\right]$
$\boldsymbol{\frac{1}{r_2}}$	$\frac{TD^2V_g^2}{LV_O^2}$	$\frac{T}{4n^2L}$	$\frac{TN}{4n^2L}$	$\frac{TV_O}{4n^3LV_g}$

$$G_{og\ \mathrm{DCM}}=\left.\frac{\hat{v}_O}{\hat{v}_g}\right]_{\hat{d}=0}=\frac{\frac{TD^2V_o^2R_L}{R_LTD^2V_g^2+LV_o^2}\left(\frac{2V_g}{V_o}-\frac{1}{n}\right)}{1+\frac{LV_o^2R_L}{R_LTD^2V_g^2+LV_o^2}Cs}. \quad (11)$$

As (10) and (11) show, G_{od} and G_{og} are first order transfer functions, with a pole in the left-half plane. A comparative analysis of these results with the transfer functions obtained for the PSFB converter when operating in DCM reveals that they will coincide if the value of the PSFB converter output filter inductor is the same as the value of the SAB inductor placed on the transformer secondary side. It should be noted that the SAB converter inductor has been placed on the transformer primary side in the analysis carried out so far (see Fig. 1) and, therefore, its value will be $n^2 \cdot L$ if it were transferred to the transformer secondary side.

B. Small-Signal Average Linear Model in the CCM

As stated before for the operation in the CCM, the electric charge injected into the R_LC network during a switching half-period depends on the value of i_D at the end of the previous switching half-period [see Fig. 2(a)]. This is because i_L does not start at zero, as occurs in the DCM [see Fig. 2(b)]. Therefore, a change in the control variable (d) in a given switching half-period does not determine a new and unique value of injected electric charge for the next switching half-periods. In fact, the value of the electric charge injected into the R_LC network will be changed during a certain number of switching half-periods after reaching its final steady-state value. The next step toward finding out a small-signal linear model for the SAB converter in CCM must be the determination of that certain number of switching periods needed to reach the aforementioned steady-state value.

1) Study of the Perturbation of the Transferred Electric Charge Corresponding to a Change in the Duty Cycle Value: Only d can change appreciably in a switching half-period. Input and output voltages are maintained constant (with a small ripple) during several switching half-period due to the large value of the input and output capacitors. Consequently, when d is modified, the slopes of the currents shown in Fig. 2 do not change. Only the duration of some intervals is modified when d changes. Fig. 6 analyzes the evolution of i_D in these circumstances. In this figure, three waveforms corresponding to i_D have been represented together. The waveform in red is the actual evolution of i_D when an increase in t_c takes place, which means an increase in the converter duty cycle. The waveform in blue represents the evolution that i_D would have followed if the duty cycle had remained constant. Finally, the waveform in green shows the hypothetical waveform corresponding to have the steady-state waveform from the beginning of the perturbed switching period. It should be noted that this waveform has a discontinuity at the aforementioned switching period that actually is not possible, because it would mean a sudden variation of i_L.

As can be seen in the example given in Fig. 6, i_D reaches its almost final value after finishing one complete switching period and, consequently, the transferred electric charge reaches its steady-state value at that time. However, this is only an example and it must be determined whether this conclusion can be extended to other cases with different specifications.

As can be observed in Fig. 6, changes in d determine variations of t_c and indirectly changes in the maximum value of i_D (as designated as i_{D1} in Fig. 6), in the value of i_D where the ramp changes its slope (called i_{D2}) and in the instants when i_D reaches zero (designated as t_2). The value of the perturbations of these quantities in each half-period can be carefully computed for m consecutive half-periods. The generalized expressions, thus, obtained for the increments of i_{D1}, i_{D2}, and t_2 in the m half-periods are

$$\widehat{i_{D1\_m}}=\frac{1}{2}\,\frac{V_g\,(1-N)}{L}\,\frac{(1+N)^{m-1}+(N-1)^{m-1}}{(1+N)^{m-1}}\widehat{t_c} \quad (12)$$

$$\widehat{i_{D2\_m}}=\frac{V_g\,(1+N)}{2L}\,\frac{(1+N)^{m}-(N-1)^{m}}{(1+N)^{m}}\widehat{t_c} \quad (13)$$

$$\widehat{t_{2\_m}}=\frac{1}{2}\,\frac{(1+N)^{m}-(N-1)^{m}}{(1+N)^{m}}\widehat{t_c} \quad (14)$$

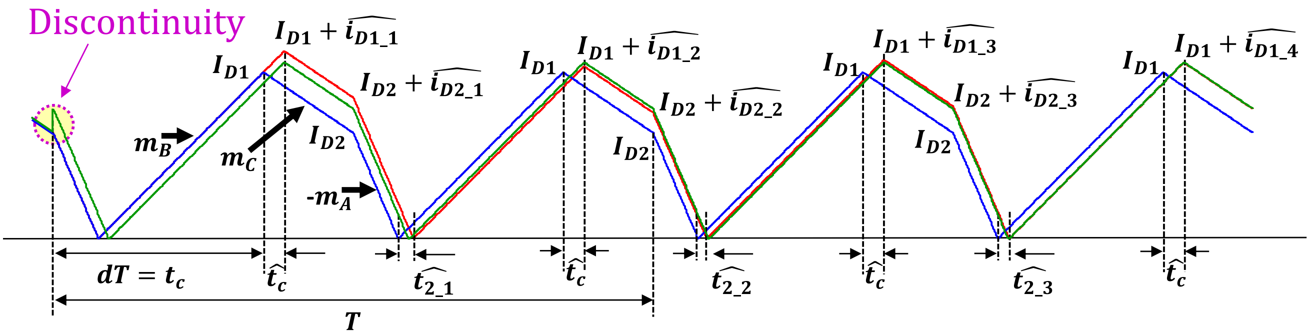

Fig. 6. Evolution of i_D after a duty cycle perturbation.

where N is the normalized voltage conversion ratio, defined as

$$N = \frac{V_O}{nV_G}. \tag{15}$$

The analysis carried out to obtain (12), (13), and (14) is fully detailed in the Appendix.

Due to the changes in i_{D1}, i_{D2}, and t_2, the electric charge injected into R_LC (designed as q_D) also changes. The increment of q_D in the m half-period can be calculated from (12), (13), and (14) after a laborious process. The result is

$$\widehat{q_{D\_m}} = \frac{V_gT}{4nL}\left[1-2D-\frac{(N-1)^m}{(1+N)^{m-1}}\right]\widehat{t_c}. \tag{16}$$

The limit of $\widehat{q_{D\_m}}$ when m tends to infinity is

$$\widehat{q_{D\_\infty}} = \lim_{m\to\infty}\widehat{q_{D\_m}} = \frac{V_gT}{4nL}\left[1-2D\right]\widehat{t_c}. \tag{17}$$

The average value of $\widehat{q_{D\_m}}$ during h half-periods can be computed from (17) as follows:

$$\begin{aligned}\widehat{q_{D\_m\_h}} &= \frac{1}{h}\left(\sum_{m=1}^{m=h}\widehat{q_{D\_m}}\right) = \frac{V_gT}{4nL}\left[1-2D-Err\left(N,h\right)\right]\\ \widehat{t_c} &= \widehat{q_{D\_\infty}} - \left[\frac{V_gT}{4nL}Err\left(N,h\right)\right]\widehat{t_c}\end{aligned} \tag{18}$$

where

$$Err\ (N,h) = \frac{1}{h}\sum_{m=1}^{m=h}\frac{(N-1)^m}{(1+N)^{m-1}}. \tag{19}$$

After comparing (17) and (18), we can conclude that Err(N,h) determines the difference between the increment of average electric charge injected into R_LC in h half-periods and the value of this increment in steady state. The values of Err(N,h) for different values of N and h are shown in Table II.

In order to evaluate the influence of Err(N,h) in (18), its value must be compared with the term 1-2D. It should be noted that, for common values of D, values of Err(N, h) are negligible in comparison with the term 1-2D after a few switching periods. As an example, if D = 0.35, then 1-2D = 0.3 and the SAB converter operates in CCM for values of N < 2D = 0.7, according to [7]. As can be seen in Table II, the values of Err(N, h) are much lower than 0.3 after a few switching periods.

TABLE II
VALUES OF ERR(N,H)

	h=4 (2 switching periods)	**h=6 (3 switching periods)**	**h=8 (4 switching periods)**
N=0.1	0.057	0.050	0.044
N=0.2	0.076	0.060	0.048
N=0.4	0.071	0.050	0.037
N=0.6	0.050	0.033	0.025
N=0.8	0.025	0.017	0.012

It can be concluded that, although a perturbation in d does not imply an instantaneous change of the injected electric charge into R_LC in the case of the CCM, the delay between both variations is very short, since the steady state is achieved within a few switching periods. Thanks to this important conclusion, the same process applied to obtain the small-signal linear model in the case of the DCM can be extended to the case of the CCM.

2) Proposed Small-Signal Linear Model in the CCM: The linearization of the current sources given by (5) and (6) around an operating point, results in the same canonical circuit given in Fig. 4. However, the value of the parameters defining the current sources and the resistors are different in both conduction modes. These new parameter values are also given in Table I (right-side column). As the canonical small-signal linear circuit shown in Fig. 4 is also valid in the CCM, the transfer functions (7) and (8) are also valid in this case, but with the new parameters corresponding to the CCM. Consequently, both conduction modes have first order small-signal average linear models, but with different values of their parameters. From the values of j_2, g_2 and r_2 given in Table I for the CCM, (7) and (8) become

$$G_{od\ \mathrm{CCM}} = \left.\frac{\hat{v}_O}{\hat{d}}\right]_{\hat{v}_g=0} = \frac{\frac{R_L4n^2V_g^2T}{2(R_LTV_o+4n^3LV_g)}\left(1-2D\right)}{1+\frac{R_L4n^3LV_g}{R_LTV_o+4n^3LV_g}Cs} \tag{20}$$

$$G_{og\ \mathrm{CCM}} = \left.\frac{\hat{v}_O}{\hat{v}_g}\right]_{\hat{d}=0} = \frac{\frac{R_L4n^2V_g^2T}{2(R_LTV_o+4n^3LV_g)}\left(1-2D\right)}{1+\frac{R_L4n^3LV_g}{R_LTV_o+4n^3LV_g}Cs}. \tag{21}$$

TABLE III
SIMULATION AND EXPERIMENTAL SETUP PARAMETERS

Parameter	Value
Input voltage (v_g)	800 – 850 V
Output voltage (v_o)	350 – 400 V
Switching period (T)	30 μs
Average output current (i_{D_avg})	0.5 – 5.5 A
Transformer turns ratio (n)	1
Inductor (L)	408 μH
Output capacitor (C)	32.9 μF

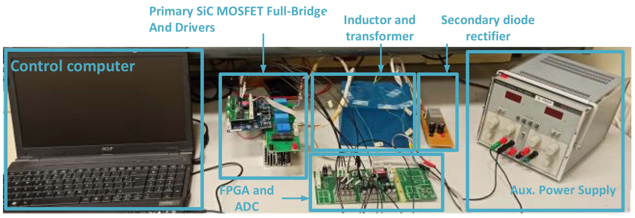

Fig. 7. Experimental prototype.

C. Comparison of the Parameters of the Small-Signal Linear Models in the Boundary Between Modes

As mentioned before, Table I shows that the value of a given parameter in the DCM differs from the value of the same parameter in the CCM.

As stated in [7], the boundary between both conduction modes occurs when $N = V_o/(nV_g) = 2D$. Taking into account this relationship, the value of the canonical circuit parameters can be calculated for the boundary condition, either coming from the DCM (left-hand side) or coming from the CCM (right-hand side). The values, thus, obtained for each parameter at the boundary are different, as the central columns of Table I show. Therefore, the parameters of the canonical circuit have an abrupt change at the boundary between conduction modes. This behavior, related to the change of the average small-signal linear model when the conduction mode changes, also takes place in other converters.

IV. SIMULATION AND EXPERIMENTAL RESULTS

The average models proposed for the SAB converter in both conduction modes are validated using simulation and experimental results. An ideal SAB converter, simulated with PSIM, and a preliminary experimental prototype, based on SiC MOSFETS and diodes, were designed and developed using the design guide proposed in [7] with the specifications of Table III.

A. Validation of the Proposed Average Model

The average model proposed in Section II (see Fig. 3) is validated using simulation and experimental results. As simulation and analytical results match perfectly, only analytical results will be compared with experimental results. Fig. 7 shows a picture of the experimental setup used to obtain the experimental results. The prototype has been designed according to the design procedure given in [7].

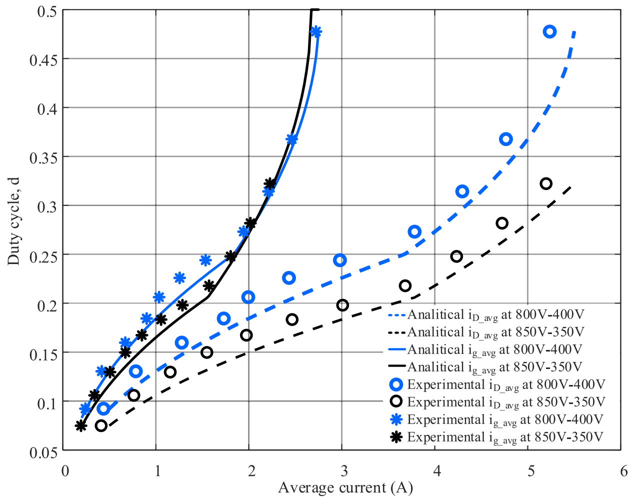

Fig. 8. Analytical and experimental results of the average input and output current, in both conduction modes, and for the extreme values of input and output voltage.

TABLE IV
THEORETICAL, SIMULATED AND EXPERIMENTAL VALUES OF $\widehat{i_{D1\_m}}$ FOR 5 CONSECUTIVE HALF-PERIODS

$\widehat{i_{D1\_m}}$ (A)	$\widehat{i_{D1\_1}}$	$\widehat{i_{D1\_2}}$	$\widehat{i_{D1\_3}}$	$\widehat{i_{D1\_4}}$	$\widehat{i_{D1\_5}}$
Theoretical	1.654	0.504	0.954	0.776	0.847
Simulated	1.653	0.504	0.948	0.777	0.841
Experimental	1.630	0.767	1.202	0.985	1.060

The value of N is 0.438.

To verify the proposed model shown in Fig. 3, the SAB converter prototype has been connected in between two external voltage sources (Keysight N8957A and N8762A). The converter duty cycle is changed, and the corresponding values of the average input and output currents have been measured using Fluke 87V multimeters. This procedure has been repeated for different values of the input and output voltages, according to Table III. The results, thus, obtained are shown in Fig. 8, where very good agreement between analytical and experimental results can be observed. The slight differences between them are due to the existing power losses in the prototype. Consequently, the actual duty cycle measured in the prototype is slightly higher than the predicted one. Moreover, the intervals of concavity in the curves shown in Fig. 8 correspond to operate in the DCM, whereas those of convexity correspond to operate in the CCM.

B. Validation of the Approximation Proposed for the Small-Signal Model in CCM

As previously stated in Section III for a change in the duty cycle of a SAB converter operating in the DCM, i_{D_avg} reaches its final value in the next switching half-period after the change. However, i_{D_avg} reaches its final value after a few switching periods when the converter operates in the CCM, as will be validated by simulation and experimental results in this section.

Table IV shows theoretical, simulated and experimental results obtained in the prototype of SAB converter whose specifications are listed in Table III. The perturbed values of i_{D1}

TABLE V
THEORETICAL, SIMULATED AND EXPERIMENTAL VALUES OF PARAMETER J_1 AND J_2 OF THE CANONICAL CIRCUIT IN BOTH CONDUCTION MODES

	DCM theor.	**DCM simul.**	**DCM exper.**	**CCM theor.**	**CCM simul.**	**CCM exper.**
j_1 (A)	12.61	13.11	10.27	5.61	5.58	5.84
j_2 (A)	28.81	26.11	23.35	12.82	13.05	12.74

in five half-periods are used in Table IV to compare theoretical, simulated and experimental results, showing good agreement between them. These results have been obtained when the value of d changes from 0.25 to 0.30 and the values of the input and output voltage are 800 V and 350 V, respectively. The theoretical values for $\widehat{i_{D1\_m}}$ have been obtained using (12), whereas the simulated and experimental values have been computed as the difference of i_{D1} in each half-period and the previous one. As can be seen, theoretical and simulation results match perfectly, whereas small differences are detected in the experimental results, due to small parasitic oscillations in the peak value of i_{D1}. However, the measured values follow the expected tendency. Moreover, the steady state is almost reached in only five half-periods.

Fig. 9 shows simulated and experimental evolution of i_D after the abovementioned change in the duty cycle, i.e., $\hat{d} = \Delta d = 0.3\text{-}0.25 = 0.05$. Shown in Fig. 9(a) for operation in the DCM, the i_D waveform changes instantly after the duty cycle change that takes place after 0.04 ms. The value of i_{D1} is 4.63 A before the duty cycle change, whereas it reaches the final value of 6.28 A the next switching period after the duty cycle change.

The case of operation in the CCM is shown in Fig. 9(b). The value of i_{D1} is 7.59 A before the duty cycle change. After the duty cycle change, the value of i_{D1} oscillates between a maximum value of 9.24 A and a minimum one of 8.09 A, reaching the steady-state value of approximately 8.41 A after four switching periods (eight half-periods). It should be noted that the effect of the duty cycle change on the output voltage depends on the area determined by the i_D waveform (i.e., the electric charge injected into R_LC). As can be observed in Fig. 9, areas corresponding to values of i_{D1} higher than its steady-state value are rapidly compensated by areas corresponding to values of i_{D1} lower than that steady-state value, thus leading to inject the new value of electric charge in a few switching periods.

Although simulation and experimental results show good agreement, there are some disparities between both waveforms. In Fig. 9(b), a current spike appears at the peak of the experimental current waveform. This spike is due to the hard turn-OFF of one of the primary side switches and the start conducting of the other switch placed in the same leg, e.g., S_1 and DS_2.

Moreover, additional resonances appear when i_D reaches zero in the case of waveforms corresponding to operate in DCM [see Fig. 9(a)]. This is a well-known effect, mainly due to the parasitic capacitance of the output diodes.

C. Validation of the Proposed Small-Signal Linear Model

This section shows a comparison of the theoretical, simulated and experimental values of parameters j_1 and j_2 (see Fig. 4) in both conduction modes. As this table shows, all the values are in good agreement, especially the theoretical and the simulated ones.

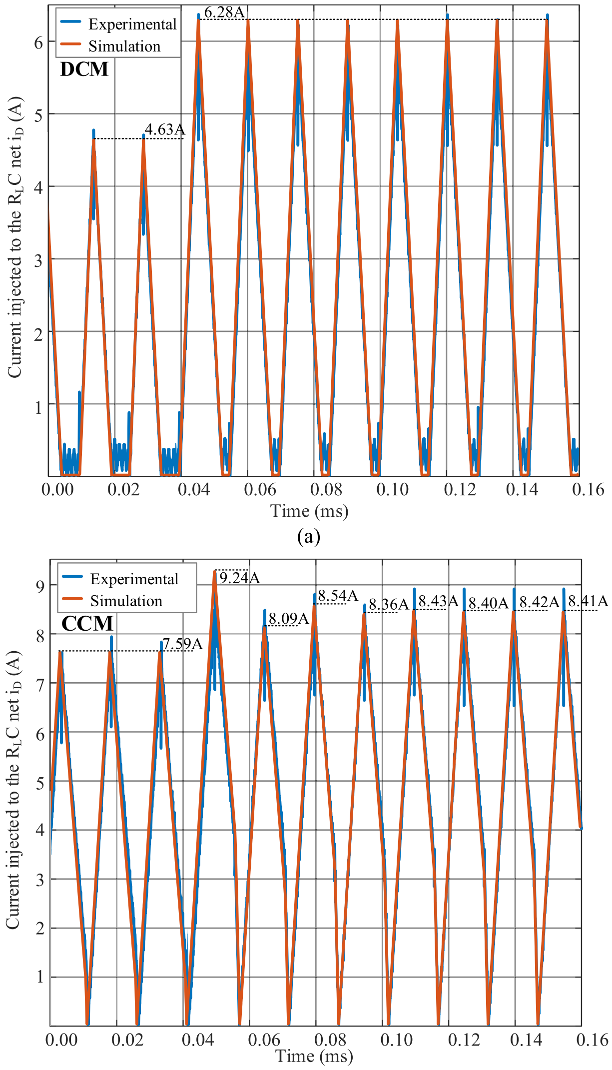

(a)

(b)

Fig. 9. Experimental and simulation results of i_D for a step change in duty cycle $\hat{d} = \Delta d = 0.05$. (a) In the DCM. (b) In the CCM. Simulated value of i_{D1} in each half-period are included.

The theoretical values of j_1 and j_2 have been obtained by using the equations given in Table I. The steady-state values of the duty cycle (i.e., D) are 0.190 in the DCM and 0.282 in the CCM. Simulated and experimental values of j_1 and j_2 (see Table V) have been obtained as follows. The values of the input and output voltage are fixed at 800 V and 350 V, respectively, by connecting voltage sources in both ports. For operation in the DCM, duty cycle d is changed around its steady-state value 0.190, from 0.182 to 0.199. In the case of operation in the CCM, the change takes place around 0.282, from 0.243 to 0.321. The values of j_1 and j_2 have been computed as follows:

$$j_1 = \frac{\Delta i_{g\_avg}}{\Delta d} = \frac{i_{g\_avg}\left(d_{\text{final}}\right) - i_{g\_avg}\left(d_{\text{initial}}\right)}{d_{\text{final}} - d_{\text{initial}}} \tag{22}$$

TABLE VI
THEORETICAL, SIMULATED, AND EXPERIMENTAL VALUES OF PARAMETERS G_1, G_2, R_1, AND R_2 IN BOTH CONDUCTION MODES

	DCM theor.	**DCM simul.**	**DCM exper.**	**CCM theor.**	**CCM simul.**	**CCM exper.**
g_1 (Ω^{-1})	-0.0024	-0.0025	-0.0025	0.0013	0.0013	0.0016
g_2 (Ω^{-1})	0.0088	0.0093	0.0097	0.0085	0.0081	0.0098
r_1 (Ω)	410.58	476.19	684	634.31	555.55	657.05
r_2 (Ω)	80.85	87.72	76.06	122.59	114.94	115.19

TABLE VII
SPECIFICATIONS FOR THE TIME-DOMAIN AND THE FREQUENCY-DOMAIN TESTS

Parameter	Value in DCM	Value in CCM
Input voltage (v_g)	800 V	800 V
Initial output voltage (v_o)	350 V	350 V
Load resistance (R_L)	137.3	79.4
Initial duty cycle (d)	0.185	0.271

$$j_2 = \frac{\Delta i_{D\_avg}}{\Delta d} = \frac{i_{D\_avg}\left(d_{\text{final}}\right) - i_{D\_avg}\left(d_{\text{initial}}\right)}{d_{\text{final}} - d_{\text{initial}}}. \qquad (23)$$

A similar procedure has been followed to determine the theoretical, simulated and experimental values of g_1, g_2, r_1, and r_2, as given in Table VI. Theoretical values are also derived from Table I. The parameters shown in this table have been computed from the following steady-state values: $V_g = 805$ V and $V_o = 355$ V for the input and output voltage, $D = 0.182$ for the duty cycle when operating in the DCM and $D = 0.243$ for the case of operation in the CCM.

Simulated and experimental values of g_1 and r_2 have been obtained with $V_g = 800$ V and changing the value of v_o from 350 V to 360 V. Similarly, g_2 and r_1 have been obtained with $V_o = 350$ V and changing the value of v_g from 800 V to 810 V. The duty cycle values selected for each conduction mode are the same as the ones used for the theoretical calculations. The equations used to determine these parameters are

$$g_1 = \frac{\Delta i_{g\_avg}}{\Delta V_O}\ ;\ g_2 = \frac{\Delta i_{D\_avg}}{\Delta V_g} \qquad (24)$$

$$\frac{1}{r_1} = \frac{\Delta i_{g\_avg}}{\Delta V_g}\ ;\ \frac{1}{r_2} = -\frac{\Delta i_{D\_avg}}{\Delta V_O}. \qquad (25)$$

As Table VI shows, good agreement between theoretical, simulated, and experimental results has been always reached.

The proposed model has also been verified in the time domain. Thus, Fig. 10 shows the theoretical and experimental evolution of v_O after a step in duty cycle $\hat{d} = \Delta d = 0.005$. The evolution shown in Fig. 10(a) corresponds to operation in the DCM, whereas the one given in Fig. 10(b) corresponds to the CCM. The main conditions corresponding to this test are shown in Table VII. The input voltage was maintained constant at 800 V, whereas the load value was adjusted until reaching 350 V at the output for the duty cycle values corresponding to both conduction modes, i.e., 0.185 for the DCM and 0.271 for the CCM.

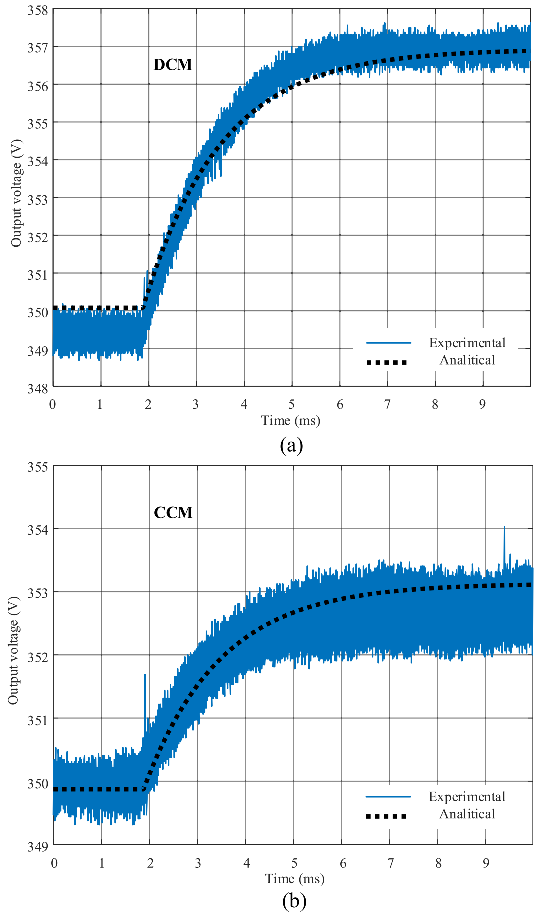

(a)

(b)

Fig. 10. Experimental and analytical response of the output voltage (v_O) for a step change in duty cycle $\hat{d} = \Delta d = 0.005$. (a) In the DCM. (b) In the CCM.

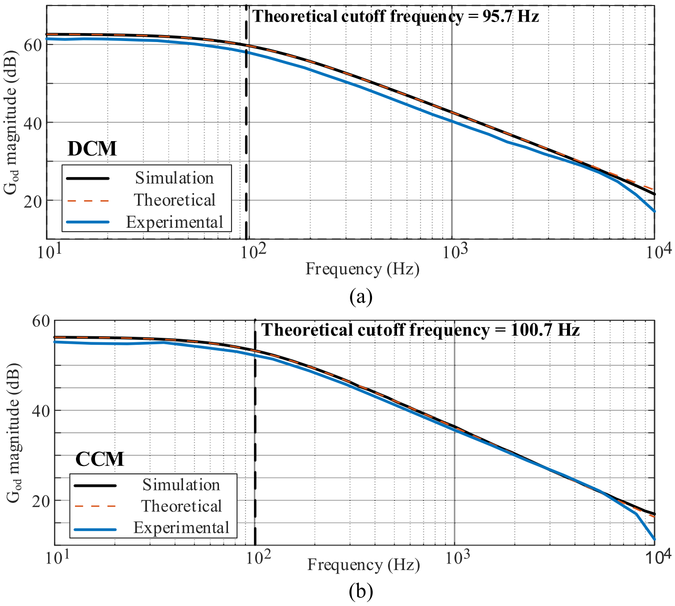

(a)

(b)

Fig. 11. Magnitude Bode plots for G_{od}. (a) In the DCM. (b) In the CCM.

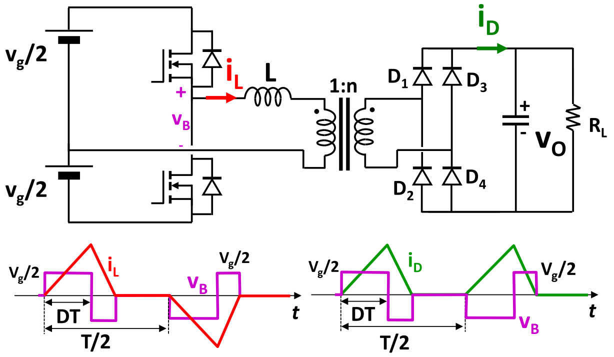

Fig. 12. SAHB simplified schematic.

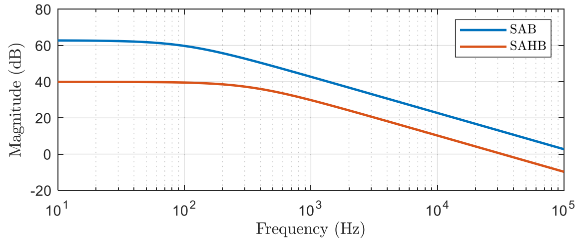

Fig. 13. Magnitude Bode plots of G_{od} for the SAHB and the SAB converters working at the same operating point.

In both conduction modes, a good agreement between theoretical and experimental results is observed, thus demonstrating the accuracy of first order model for both conduction modes.

Moreover, the proposed model has also been verified in the frequency domain. Fig. 11 shows the magnitude plots of duty cycle-to-output voltage transfer functions G_{od}, for the DCM [see Fig. 11(a)] and for the CCM [see Fig. 11(b)]. The conditions for this test were the same as the ones for the time-domain test (see Table VII). The theoretical response was calculated from (10) (DCM case) and (20) (CCM case), whereas the simulated results were obtained using PSIM, and the experimental results were measured using a Venable Frequency Response Analyzer (FRA6340). The function generator and one measurement channel of the FRA6340 are connected together to the input of an external ADC, whose output is connected to the FPGA that controls the converter. To capture the output voltage response, the other measurement channel of the FRA6340 is connected in parallel to the load. The bandwidth, delay and resolution of the ADC are not considered relevant, as the ADC characteristics surpasses considerably the test requirements. Moreover, the gain introduced by the ADC is compensated in the measuring process. As Fig. 11 shows, theoretical and simulation results match perfectly up to 10 kHz, which is one third of the switching frequency. Regarding the experimental results, a slightly lower gain is observed due to power losses and component tolerances, but these results follow the same tendency as the theoretical and simulated ones, with very good agreement. Again, a first order model response for both conduction modes is observed after analysing the converter response in the frequency domain. As such, a simple PI compensator can be selected to regulate the converter output voltage.

V. COMPARISON WITH OTHER TOPOLOGIES

As previously commented, the behavior of the SAB converter exhibits some similarities with other topologies in certain conditions. Thus, the voltage conversion ratio of this converter in DCM closely resembles the one corresponding to the PSFB converter in the same conduction mode. In fact, both voltage conversion ratios coincide if the value of the PSFB output filter inductor is the same as the value of the SAB inductor transferred to the transformer secondary side. This similarity also extends to the buck converter in DCM in some conditions, as explained in [7]. On the other hand, the SAB converter exhibits different behavior from these converters when operating in CCM.

Regarding the dynamic response, two converters stand out due to their similarities with the SAB converter. They are the SAHB converter and the DAB converter, whose dynamics are compared below.

A. Comparison With the SAHB

As mentioned before, average and small-signal models of the SAHB converter were presented in [10]. This converter and some of its most important waveforms are represented in Fig. 12. Due to its switch arrangement in the primary-side bridge, the conduction modes in this converter differ from the ones of the SAB converter. Comparing i_L and i_D waveforms for the SHAB converter [see Fig. 12] and the same waveforms for the SAB converter in the DCM [see Fig. 2(b)], we can conclude that they are similar. However, the waveforms corresponding to the voltage generated by the switch bridge, designed as v_B in both figures, differ. Consequently, the equation that determines the relationship between the average value of i_D and d, v_g and v_o also differs. In the case of the SHAB, its value is

$$i_{D\_avg} = \frac{d^2 v_g n^2 T\left(v_g - 2v_o\right)}{L\left(2v_o + v_g n\right)} \tag{26}$$

which is different from the corresponding equation for the SAB converter in the DCM (3).

As the equation for i_{D_avg} is different for both converters, the parameters obtained after linearizing are clearly different. For example, in the case of the SAHB converter, the values of parameters j_2 and r_2 are

$$j_2 = \frac{2DV_g n^2 T\left(V_g - 2V_o\right)}{L\left(2V_o + V_g n\right)} \tag{27}$$

$$r_2 = \frac{L(2V_o + V_g n)^2}{2D^2 V_g^2 T n^2\left(n+1\right)}. \tag{28}$$

These values are different from the ones given in Table I for the SAB converter.

The different dynamic behavior of both converters is also reflected in their response in the frequency domain. Thus, Fig. 13 shows the analytical magnitude Bode plot for both converters. The operating point for this test is the same as the one given in Fig. 11(a) for the SAB converter. Both converters have the same value of output capacitor. Moreover, the SAHB converter

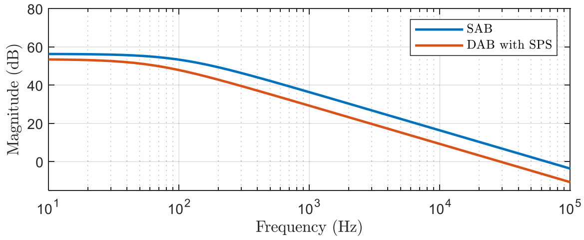

Fig. 14. Magnitude Bode plots of G_{od} for the SAB converter and for the DAB with SPS modulation.

duty cycle was adjusted to handle the same power level in both converters. As this figure shows, the Bode plots are different, with different low frequency gain and cut-off frequency.

The SAHB converter can reach a boundary mode if the inductor current does not remain at zero level during a part of the switching period. This boundary mode is designed as CCM in [10], but it differs from the CCM considered for the SAB in [7] and [8] and this article. In fact, operation in this mode implies that the switching frequency must be used to control the converter when the load changes, which is a situation completely different from the one of the SAB converter in the CCM.

B. Comparison With the DAB

Since the SAB converter can be considered as a particular case of the DAB converter, many operating points of the SAB converter can be achieved by selecting a proper DAB modulation. The simplest modulation for the DAB is the single phase-shift (SPS). This modulation consists in phase-shifting the bridges while both bridges operate at 0.5 duty cycle. In this case, the average value of i_D is

$$i_{D\_avg} = \frac{v_g \varphi_{\mathrm{DAB}} \left(\pi - |\varphi_{\mathrm{DAB}}|\right) T}{2\pi^2 Ln} \tag{29}$$

where φ_{DAB} is the phase shift between both bridges. As (29) shows, i_{D_avg} does not depend on the output voltage v_o, which is different from the case of the SAB converter, according to (3) and (5). This fact results in different small-signal linear models for the DAB converter with SPS modulation and for the SAB converter operating in any of the two possible conduction modes. For example, $1/r_2$ must be zero in the case of the DAB converter with SPS modulation due to the abovementioned lack of dependence.

The analysis in the frequency domain also shows the different dynamic behavior of both converters, as shown in Fig. 14. The operating point for this test is the same as the one given in Fig. 11(b) for the SAB converter. Both converters have the same value of output capacitor. Moreover, the DAB converter phase shift was adjusted to handle the same power level in both converters.

The behavior of the SAB converter can be replicated by selecting a more complex modulation, such as the triple phase-shift (TPS) modulation [16]. It should be noted that the SAB is controlled by phase-shifting the primary full-bridge legs. This control strategy can also be used in the case of the DAB converter. Moreover, the secondary side transistors can be controlled as if they were diodes. In one of the possible switching modes for DAB converter with TPS modulation, the average value of i_D can be expressed as follows:

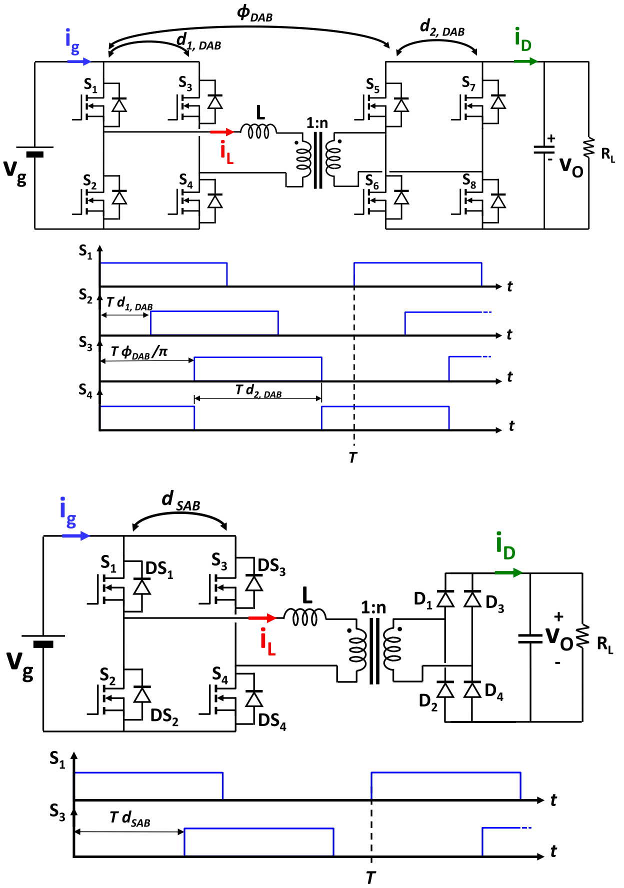

Fig. 15. Comparison of the signals used to control the DAB converter (upper part) and the SAB converter (lower part).

$$i_{D\_avg} = \frac{V_g T}{2Ln} \left[\frac{\varphi_{\mathrm{DAB}}}{\pi}\left(1 - \frac{\varphi_{\mathrm{DAB}}}{\pi}\right) - \frac{\left(2d_{1\_\mathrm{DAB}} - 1\right)^2 + \left(2d_{2\_\mathrm{DAB}} - 1\right)^2}{4} \right] \tag{30}$$

where d_{1_DAB}, d_{2_DAB}, and φ_{DAB} are defined in Fig. 15. As an example, the operation of the SAB converter in the CCM can be emulated from the DAB converter if d_{1_DAB}, d_{2_DAB}, and φ_{DAB} are selected as follows:

$$d_{1\_\mathrm{DAB}} = d \tag{31}$$

$$d_{2\_\mathrm{DAB}} = 0.5 \tag{32}$$

$$\varphi_{\mathrm{DAB}} = \frac{\pi\left(v_g n - v_o\right)}{2 v_g n}\ . \tag{33}$$

If d_{1_DAB}, d_{2_DAB}, and φ_{DAB} in (30) are replaced with the corresponding values of these quantities given by (31), (32), and (33), then the value of i_{d_avg} shown in (5) is finally obtained. Therefore, the DAB converter can mimic the behavior of the

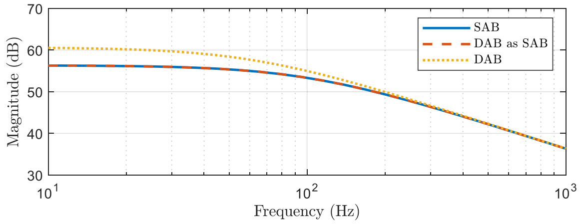

Fig. 16. Magnitude Bode plots of G_{od} for a SAB converter, a DAB converter emulating the SAB and a DAB converter with TPS modulation.

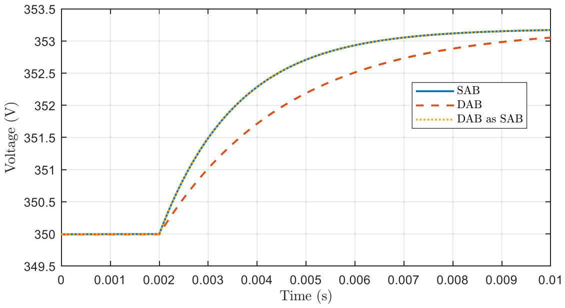

Fig. 17. Output voltage response after a step in the duty cycle in the cases of a SAB converter, DAB converter emulating the SAB and a DAB converter with TPS modulation.

SAB converter if the specific modulation conditions described above have been selected. Otherwise, the behavior of both converters is clearly different, including any small-signal linear model obtained by linearizing i_{d_avg}.

The different behavior of both converters can be tested in the frequency domain when working in similar operation points. For this purpose, three analytical magnitude Bode plots corresponding to the transfer function of G_{od} are depicted in Fig. 16. One of them corresponds to the SAB converter, whereas the others correspond to the DAB converter. One of the DAB converter plots have been obtained when this converter emulates the SAB, as previously explained. As expected, both Bode plots coincide. The third Bode plot has been obtained using a case of TPS modulation, using d_{1_DAB} as control variable, whereas d_{2_DAB} and φ_{DAB} remain constant. As Fig. 16 shows, this Bode plot differs from the others.

Also, the time-domain response can be used to highlight the aforementioned differences, as Fig. 17 shows. The operating point corresponding to this figure is the same as the one corresponding to Fig. 10(b). In the case of the SAB converter, $\hat{d} = \Delta d = 0.00500$. Regarding the DAB converter emulating the SAB behavior, the same value must be selected for the control variable step, which means $\widehat{d_{1\_DAB}} = \Delta_{d1\_DAB} = 0.00500$. On the other hand, $\widehat{d_{1\_DAB}} = \Delta_{d1\_DAB} = 0.00305$ in the case of the DAB converter with the abovementioned TPS modulation. This value has been selected in order to achieve the same final value of output voltage. Fig. 17 shows that the transient response of v_o differs in the latter case, in spite of tending to the same final value.

VI. CONCLUSION

In this article, the dynamic behavior of the SAB converter has been thoroughly studied in both conduction modes. Average and small-signal linear models have been proposed and validated using simulation and experimental results.

When operating in the DCM, the small-signal linear model corresponds to a first order system, with a pole in the left-half plane.

In the case of operation in the CCM, a higher order model could be theoretically expected, because the value of the current through the inductor at the beginning of each switching half-period is not zero (in contrast to the case of operating in the DCM), but it depends on its final value in the previous half-period. However, it has been proved that the inductor current tends to its final value in a few switching periods when a duty cycle perturbation takes place. Consequently, an almost instantaneous change in the electric charge injected into the output $R_L C$ network can be considered after the abovementioned perturbation. Due to this, the dynamic behavior of the SAB converter in the CCM can also be approximated by a first order model, similar to the case of the DCM, but with different values for its parameters.

The DCM and the CCM models have been verified by simulation and by experimental results. Finally, the small-signal models obtained for the SAB converter have been compared with those previously proposed for other similar converters, highlighting the differences between them.

APPENDIX

In this Appendix, the laborious analysis carried out to obtain 12, 13, and 14 is explained in detail. Fig. 6 shows the evolution of i_D when a change in the duty cycle take place. This figure is also useful to show the nomenclature used in this appendix.

The value of the current slopes, m_A, m_B, and m_C, can be easily obtained because input and output voltages remain almost constant in a switching period, due to the input and output capacitors. Only an output capacitor has been represented in Fig. 1, but an input capacitor is always connected in parallel with V_g. Therefore

$$m_A = \frac{1}{L}\left(V_g + \frac{V_o}{n}\right) = \frac{V_g}{L}\,(1+N) \tag{A1}$$

$$m_B = \frac{1}{L}\left(V_g - \frac{V_o}{n}\right) = \frac{V_g}{L}\,(1-N) \tag{A2}$$

$$m_C = -\frac{V_o}{Ln} = -\frac{V_g}{L}N. \tag{A3}$$

When the converter duty cycle changes due to an increase of t_c, the following relationships are verified in the first half-period after this change:

$$m_B = \frac{\widehat{i_{D1\_1}}}{\hat{t}_c} \tag{A4}$$

$$m_C = \frac{i_{D1} + \widehat{i_{D1_{1}}} - \left(i_{D2} + \widehat{i_{D2\_1}}\right)}{\frac{T}{2} - t_c - \widehat{t_c}} = \frac{\widehat{i_{D1\_1}} - \widehat{i_{D2\_1}}}{-\widehat{t_c}} \tag{A5}$$

$$m_A = \frac{\widehat{i_{D2\_1}}}{\widehat{t_{2\_1}}}. \tag{A6}$$

Using (A4), (A5), and (A6), the variations of t_2 in the first half-period can be obtained

$$\widehat{i_{D1\_1}} = m_B\, \widehat{t_c} \tag{A7}$$

$$\widehat{i_{D2\_1}} = (m_B - m_C)\, \widehat{t_c} \tag{A8}$$

$$\widehat{t_{2\_1}} = \frac{(m_B - m_C)}{m_A}\, \widehat{t_c} = \frac{1}{(1+N)}\, \widehat{t_c}. \tag{A9}$$

Following a similar procedure, the variations of t_2 in next half-periods can be computed as

$$\widehat{t_{2\_2}} = \frac{2N}{(1+N)^2}\, \widehat{t_c} \tag{A10}$$

$$\widehat{t_{2\_3}} = \frac{1+3N^2}{(1+N)^3}\, \widehat{t_c} \tag{A11}$$

$$\widehat{t_{2\_4}} = \frac{4N+4N^3}{(1+N)^4}\, \widehat{t_c}. \tag{A12}$$

Analyzing the numerator of the previous variations of t_2 for different half-periods, a general equation can be obtained using the binomial theorem (or Newton´s binomial theorem)

$$(a \pm b)^n = \binom{n}{0} a^n \pm \binom{n}{1} a^{n-1} b \pm \binom{n}{2} a^{n-2} a^2 \pm \cdots \pm \binom{n}{n} b^n \tag{A13}$$

where the coefficients are given by the Pascal´s triangle or can be calculated using the generalized Newton´s binomial theorem. The final result is

$$\widehat{t_{2\_m}} = \frac{1}{2}\, \frac{(1+N)^m - (N-1)^m}{(1+N)^m}\, \widehat{t_c}. \tag{A14}$$

A similar procedure is followed to obtain the variations of i_{D1}. Using (A7) and (A2), its value in the first half-period is

$$\widehat{i_{D1\_1}} = \frac{1}{L}\left(V_g - \frac{V_o}{n}\right) \widehat{t_c} = \frac{V_g\,(1-N)}{L}\, \frac{1}{(1+N)^0}\, \widehat{t_c}. \tag{A15}$$

The value of the variations of i_{D1} in the next half-period can be expressed as

$$\widehat{i_{D1\_2}} = \frac{V_g\,(1-N)}{L} \cdot \frac{N}{(1+N)}\, \widehat{t_c} \tag{A16}$$

$$\widehat{i_{D1\_3}} = \frac{V_g\,(1-N)}{L} \cdot \frac{1+N^2}{(1+N)^2}\, \widehat{t_c} \tag{A17}$$

$$\widehat{i_{D1\_4}} = \frac{V_g\,(1-N)}{L} \cdot \frac{3N+N^3}{(1+N)^3}\, \widehat{t_c}. \tag{A18}$$

Again, a general equation of the variations of i_{D1} in the m half-period can be obtained using the binomial theorem. The final expression for $\widehat{i_{D1\_m}}$ is

$$\widehat{i_{D1\_m}} = \frac{1}{2}\, \frac{V_g\,(1-N)}{L}\, \frac{(1+N)^{m-1} + (N-1)^{m-1}}{(1+N)^{m-1}}\, \widehat{t_c}. \tag{A19}$$

The generalized equation for the variations of i_{D2} in the m half-period can be directly obtained using geometrical constructions

$$\widehat{i_{D2\_m}} = m_A \cdot \widehat{t_{2\_m}}. \tag{A20}$$

Finally, from (A1) and (A14), (A20) becomes

$$\widehat{i_{D2\_m}} = \frac{V_g\,(1+N)}{2L}\, \frac{(1+N)^m - (N-1)^m}{(1+N)^m}\, \widehat{t_c}. \tag{A21}$$

REFERENCES

[1] R. W. A. A. De Doncker, D. M. Divan, and M. H. Kheraluwala, “A three-phase soft-switched high power-density DC/DC converter for high-power applications,” *IEEE Trans. Ind. Appl.*, vol. 27, no. 1, pp. 63–73, Jan./Feb. 1991.

[2] M. H. Kheraluwala, R. W. Gascoigne, D. M. Divan, and E. D. Baumann, “Performance characterization of a high-power dual active bridge dc-to-dc converter,” *IEEE Trans. Ind. Appl.*, vol. 28, no. 6, pp. 1294–1301, Nov./Dec. 1992.

[3] A. Rodríguez, J. Sebastián, D. G. Lamar, M. M. Hernando y, and A. Vázquez, “An overall study of a dual active bridge for bidirectional DC/DC conversion,” in *Proc. IEEE Energy Convers. Congr. Expo.*, 2010, pp. 1129–1135.

[4] A. Rodríguez, A. Vázquez, D. G. Lamar, M. M. Hernando y, and J. Sebastián, “Different purpose design strategies and techniques to improve the performance of a dual active bridge with phase-shift control,” *IEEE Trans. Power Electron.*, vol. 30, no. 2, pp. 790–804, Feb. 2015.

[5] K. Park and Z. Chen, “Control and dynamic analysis of a parallel-connected single active bridge DC–DC converter for DC-grid wind farm application,” *IET Power Electron.*, vol. 8, no. 5, pp. 665–671, 2015, doi: 10.1049/iet-pel.2014.0420.

[6] C. Sommer, A. Mertens, I. Larrazabal, and I. Kortazar, “Analytical investigation of the three-phase single active bridge for offshore applications,” in *Proc. 18th Eur. Conf. Power Electron. Appl.*, Sep. 2016, pp. 1–10, doi: 10.1109/EPE.2016.7695590.

[7] A. Rodriguez et al., “An overall analysis of the static characteristics of the single active bridge converter,” *Electronics*, vol. 11, no. 4, Jan. 2022, Art. no. 4.

[8] C. Fontana, M. Forato, M. Bertoluzzo y, and G. Buja, “Design characteristics of SAB and DAB converters,” in *Proc. Inter. Aegean Conf. Elect. Machines Power Electron.*, 2015, pp. 661–668.

[9] A. Averberg and A. Mertens, “Characteristics of the single active bridge converter with voltage doubler,” in *Proc. 13th Int. Power Electron. Motion Control Conf.*, Poznan, Poland, 2008, pp. 213–220.

[10] G. D. Demetriades, “On small-signal analysis and control of the single- and the dual-active bridge topologies,” Doctoral Dissertation, Royal Institute of Technology, Sweden, ISBN-91-7283-966-x, 2005.

[11] H. Qin and J. W. Kimball, “Generalized average modeling of dual active bridge DC–DC converter,” *IEEE Trans. Power Electron.*, vol. 27, no. 4, pp. 2078–2084, Apr. 2012, doi: 10.1109/TPEL.2011.2165734.

[12] D. Costinett, R. Zane, and D. Maksimović, “Discrete-time small-signal modeling of a 1 MHz efficiency-optimized dual active bridge converter with varying load,” in *Proc. IEEE 13th Workshop Control Model. Power Electron.*, Kyoto, Japan, 2012, pp. 1–7, doi: 10.1109/COMPEL.2012.6251766.

[13] P. R. K. Chetty, “Current injected equivalent circuit approach to modeling of switching DC-DC converters in discontinuous inductor conduction mode,” *IEEE Trans. Ind. Electron.*, vol. IE-29, no. 3, pp. 230–234, Aug. 1982.

[14] P. R. K. Chetty, “CIECA: Application to current programmed switching dc-dc converters,” *IEEE Trans. Aerosp. Electron. Syst.*, vol. AES-18, no. 5, pp. 538–544, Sep. 1982.

[15] S. Cuk and R. D. Middlebrook, “A general unified approach to modelling switching DC-tO-DC converters in discontinuous conduction mode,” in *Proc. IEEE Power Electron. Specialists Conf.*, Jun. 1977, pp. 36–57.

[16] C. Calderon et al., “General analysis of switching modes in a dual active bridge with triple phase shift modulation,” *Energies*, vol. 11, no. 9, Sep. 2018, Art. no. 9, doi: 10.3390/en11092419.

Alberto Rodríguez (Member, IEEE) was born in Oviedo, Spain, in 1981. He received the M.Sc. degree in telecommunication engineering and the Ph.D. degree in electrical engineering from the University of Oviedo, Gijon, Spain, in 2006 and 2013, respectively.

Since 2006, he has been a Researcher Engineer and an Assistant Professor with the Department of Electrical and Electronic Engineering, University of Oviedo. Since 2018, he has been an Associate Professor. His research interests include multiple ports power supply systems, bidirectional dc–dc power converters, and wide band gap semiconductors.

Alexis A. Gómez (Student Member, IEEE) was born in Caranceja, Spain, in 1998. He received the B.Sc. degree in industrial technologies engineering and the M.Sc. degree in electrical engineering from the University of Cantabria, Santander, Spain, in 2020 and 2021, respectively.

He was a member of the Power Supply Systems Group, University of Oviedo in 2021. His research interests include focused on multiple ports power supply systems, bidirectional dc–dc power converters, and wide bandgap semiconductors.

Marta M. Hernando (Senior Member, IEEE) was born in Gijón, Spain, in 1964. She received the M.Sc. and Ph.D. degrees in electrical engineering from the University of Oviedo, Gijón, Spain, in 1988 and 1992, respectively.

She is currently a Full Professor with the University of Oviedo. Her research interests include switching-mode power supplies and high-power factor rectifiers.

Diego G. Lamar (Senior Member, IEEE) was born in Zaragoza, Spain, in 1974. He received the M.Sc. and Ph.D. degrees in electrical engineering from the University of Oviedo, Oviedo, Spain, in 2003 and 2008, respectively.

In 2003, 2005, and 2011, he was a Research Engineer, Assistant Professor, and Associate Professor, respectively, with the University of Oviedo. Since Apr. 2022, he is Full Professor with the University of Oviedo. Since 2003, he has been involved in Power Electronics, participating in more than 40 Research and Development projects. He has authored or coauthored more than 200 technical papers in journals and conferences. His main research interests include converter modelling, power-factor-correction, LED drivers, dc–dc converters for visible light communication applications and wide band-gap semiconductors in power converters.

Javier Sebastián (Life Senior Member, IEEE) was born in Madrid, Spain, in 1958. He received the M.Sc. degree in electrical engineering from the Technical University of Madrid (UPM), Madrid, Spain, in 1981, and the Ph.D. degree in electrical engineering from the University of Oviedo, Oviedo, Spain, in 1985

He was an Assistant Professor and an Associate Professor with both the UPM and the University of Oviedo. Since 1992, he has been with the University of Oviedo, where he is currently a Professor. His research interests include switching-mode power supplies, modeling of dc-to-dc converters, single-phase high power factor rectifiers, LED drivers, dc-to-dc converters for envelope tracking techniques and for visible light communication, and the use of wide band-gap semiconductors in power supplies.